J. Iron Steel Res. Int. (2019) 26:321–328
https://doi.org/10.1007/s42243-018-0144-x

ORIGINAL PAPER

Shape memory effect of dual-phase NiMnGaTb ferromagnetic shape memory alloys

Jiang Zhang[1,2] · Yong-hong Ma[1] · Ruo-lin Wu[2,3] · Jing-min Wang[2]

Received: 9 May 2018 / Revised: 31 August 2018 / Accepted: 3 September 2018 / Published online: 2 November 2018

Abstract
The evolution of microstructure, reverse martensitic transformation and the correlated influence on shape memory effect was investigated in as-cast and directionally solidified dual-phase NiMnGaTb alloys. The directionally solidified alloys exhibit single-crystal microstructure, preferred dendrite microstructure, and mussy dendrite microstructure in the specimens grown at a withdrawal rate (v) of 10, 50 and 200, and 1000 μm/s, respectively. The precipitates dispersively distribute in the martensite matrix for the directionally solidified alloys. With the refined grains and particle precipitates, the reverse martensitic transformation gradually shifts to lower temperatures and the temperature span is significantly broadened. The directional solidification technology can effectively enhance the strains recovered due to shape memory effect (ε_{sme}) and decrease the compressive stress required to trigger the reorientation of twins (σ) via the realization of preferred orientation, while the maximal ε_{sme} and minimum σ can reach 4.96% and 14 MPa in v = 10 μm/s specimens, respectively. The formation of dendrite morphology degrades the shape memory strain, and ε_{sme} decreases with the growth of secondary dendritic arms.

Keywords NiMnGaTb alloy · Directional solidification · Dual-phase microstructure · Shape memory effect

1 Introduction

Magneto-elastic materials represented by ferromagnetic shape memory alloys (FSMAs) and magnetostrictive materials have been extensively studied because of the excellent magnetostrain effect triggered by applying and removing external magnetic field [1–4]. This particular advantage compared with the conventional shape memory alloys allows them to work under high-frequency alternating magnetic field, and thus, some advanced transducers and vibration harvesting devices have been fabricated based on these new materials [5–9]. As for the mentioned two types of magneto-elastic materials, FSMAs have attracted more attention due to the larger shape memory strain and more abundant physical effects [10–16]. However, compared with the conventional NiTi alloys, the weak cohesion of the grain boundaries in the representative FSMA of NiMnGa alloys leads to the intrinsic brittleness. Therefore, the polycrystals are easily cracked under quite large compressive deformation, so the shape memory strain is unable to recover after heat treatment [17]. Previous investigations have revealed that slight addition of rare earth (RE) can significantly improve the ductility because of the formation of RE-rich precipitates [18–27]. The compressive strength of the polycrystals increases from ~ 400 MPa for ternary alloy to over 1000 MPa for Tb-doped alloy, and the compressive strain is improved from ~ 10 to ~ 20%. Simultaneously, the martensitic transformation and magnetic transition in the alloys are unaffected. This significant enhancement provides the opportunity for NiMnGaTb alloys to bear larger compressive pre-strains.

According to previous study, the optimal addition concentration of Tb is proved to be ~ 0.2 at.% [17, 19]. Both of the mechanical properties and the shape memory effect

✉ Jing-min Wang
jingmin@buaa.edu.cn

[1] Institute of Higher Education, Beihang University, Beijing 100191, China

[2] School of Materials Science and Engineering, Beihang University, Beijing 100191, China

[3] Central Iron & Steel Research Institute, Beijing 100081, China

(SME) are significantly degraded when Tb content is higher or lower than this optimal value. Although sizable shape memory strain of 2.68% can be achieved when the pre-strain is 8% for 0.2 at.% Tb–doped NiMnGa alloy, this value is still away from ideal. Sui et al. [25] utilized thermomechanical training to enhance the shape memory strain slightly, but still limited methods can effectively reach the target. Therefore, the acquisition of better shape memory performance is still needed in the alloys, and preparing single-crystal or oriented crystals may benefit it.

In this work, the directional solidification technology with different crystal growth rates was employed to prepare $Ni_{50}Mn_{29}Ga_{20.8}Tb_{0.2}$ rods, and the as-cast alloy with the same chemical composition was prepared for the contrast. The effect of directional solidification on the microstructures, crystal orientation, martensitic transformation and shape memory effect was investigated in Tb-doped quaternary alloys. Excellent shape memory effect was obtained in the directionally solidified $Ni_{50}Mn_{29}Ga_{20.8}Tb_{0.2}$ rod with optimized solidification microstructures.

2 Experimental

High-purity starting elements nickel, manganese, gallium and terbium were arc-melted for the preparation of $Ni_{50}Mn_{29}Ga_{20.8}Tb_{0.2}$ master ingots. Every ingot was re-melted four times to ensure homogeneity. Subsequently, the ingots were cast in a chilled copper mold to obtain master rods with the diameter of 7 mm. In order to prevent the burning loss during the smelting process, Ga and Tb elements were weighed for 2% excess and fully covered by the sheet iron in copper crucible. Directional solidification technology was carried out with the water-cooled stage pulling downward at a withdrawal rate of 10, 50, 200 and 1000 μm/s, respectively.

The micromorphologies were characterized by optical metallographic microscopy and electron probe microanalysis. The room-temperature phase structure and crystal orientation were characterized by X-ray diffraction (XRD) with Cu Kα radiation. The detailed morphologies were observed by transmission electron microscopy (TEM). The reverse martensitic transformation was determined by differential scanning calorimetry (DSC) measurements with the heating rate of 10 °C/min. The shape memory effect of all the alloys was tested at room temperature with the compression direction perpendicular to the undersurface of the columns, and the deformation rate was 0.02 mm/min. After unloading, the samples were heated to 200 °C for 10 min in order to recover the strains at the temperature significantly higher than the reverse martensitic transformation temperature. The heights of the samples were measured before loading (l_0), after unloading (l_1) and after heating (l_2) by a vernier caliper with an accuracy of 0.02 mm, respectively. The pre-strain was defined as $\varepsilon_{pre} = \Delta l/l_0$, where Δl represents the displacement of the crosshead. The strains which was recovered due to SME (ε_{sme}) were calculated as $(l_2 - l_1)/l_0 \times 100\%$.

3 Results and discussion

Figure 1 shows the microstructure of the as-cast $Ni_{50}Mn_{29}Ga_{20.8}Tb_{0.2}$ alloy under the optical microscope (Fig. 1a) and electron microscope (Fig. 1b), respectively. The twin structure observed in Fig. 1a proves that the matrix is martensite at room temperature, so the martensitic transformation temperature is higher than room temperature. Besides, some black points and lines can be seen in Fig. 1a, corresponding to the white phase in Fig. 1b. Based on previous studies, they are confirmed to be Tb-rich precipitates [17, 19]. This means that Tb-rich precipitates dispersively distribute in the grains and continuously along the grain boundaries in the as-cast alloys. XRD pattern of the as-cast alloy indicates that the martensite phase is a non-modulated martensite at room temperature as shown in Fig. 1c, and no preferred crystal orientation is observed. Moreover, some additional diffraction peaks can be seen in XRD pattern, which should be derived from Tb-rich precipitates.

When the directional solidification technology is performed to $Ni_{50}Mn_{29}Ga_{20.8}Tb_{0.2}$ alloy, the microstructure and preferred crystal orientation vary significantly with the increasing withdrawal rate. Figure 2a–c shows the backscattered electron (BSE) images of the cross section surface and longitudinal section surface, and the room-temperature XRD pattern of the rod grown at the withdrawal rate of $v = 10$ μm/s, respectively. No grain boundaries can be seen on the cross section surface and longitudinal section surface, which illustrates that the rod may exhibit single-crystal morphology. Compared with the as-cast alloys with the same chemical composition, the distribution of Tb-rich precipitates transforms to be completely dispersive in the directionally solidified specimen, and Tb-rich precipitates exist as particles in the matrix. Moreover, the room-temperature XRD pattern with X-ray focusing on the cross section surface suggests [100] preferred orientation of this specimen because the intensities of other diffraction peaks are very weak. These results indicate that the crystal grows stably during the directional solidification process, the misoriented grains are wept out and the main grain with the [100] preferred orientation is reserved. Therefore, the solid–liquid interface should be planar or convex in this condition.

When the withdrawal rate increases to 50 and 200 μm/s, the dendrite morphologies appear in the rods, as shown in

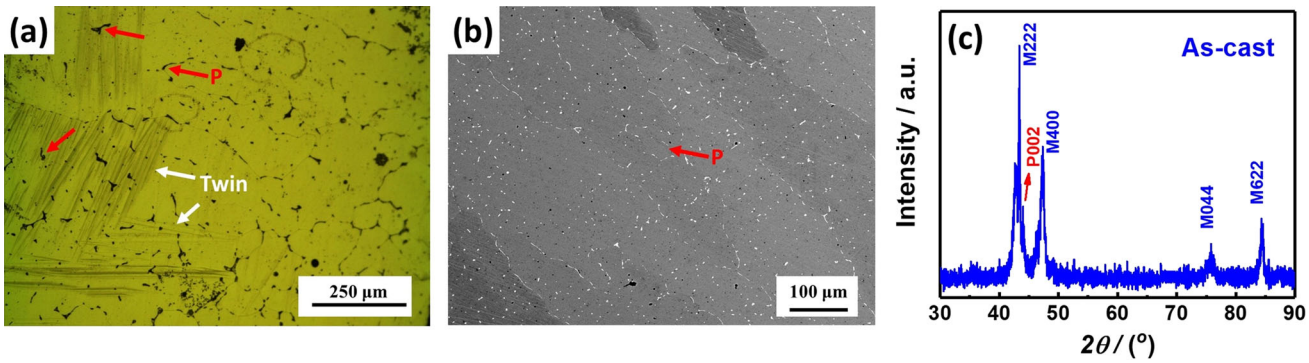

Fig. 1 Optical morphology (**a**), backscattered electron image (**b**) and room-temperature XRD pattern (**c**) of as-cast $Ni_{50}Mn_{29}Ga_{20.8}Tb_{0.2}$ alloy

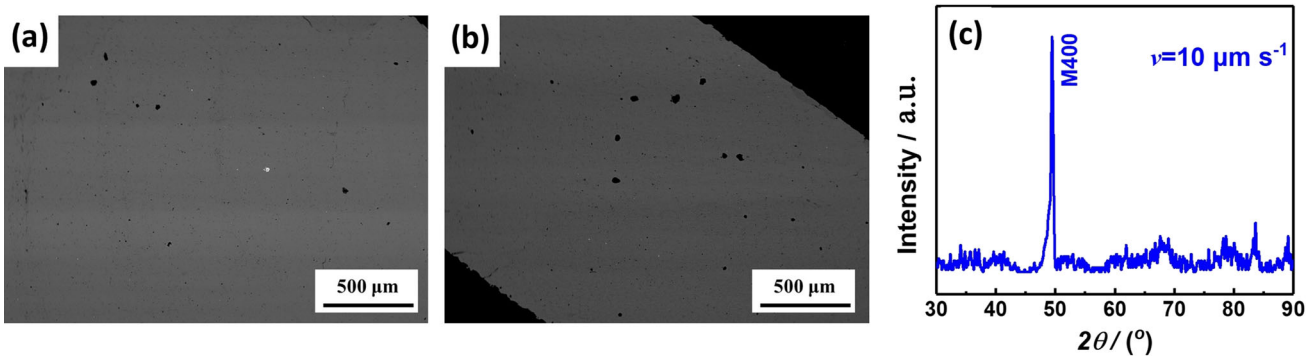

Fig. 2 BSE images of cross section surface (**a**) and longitudinal section surface (**b**) and room-temperature XRD pattern (**c**) of $Ni_{50}Mn_{29}Ga_{20.8}Tb_{0.2}$ grown at 10 μm/s

Fig. 3a, b, d, e. Obvious secondary dendrite arms can be seen, as shown in the enlarged figure shown in the inset of Fig. 3b, in which two pairs of secondary dendrite arms are formed along each primary dendrite arm. As is shown, the formation of secondary dendrite arms is attributed to the instability on the side walls of the cellular grains. That is to say, the instability of the side walls of the cellular grains has occurred under these conditions. Even so, the primary dendrite arm is still parallel to the withdrawal direction, indicating the stable growth of the dendrites. When the withdrawal rate further increases to 1000 μm/s, serious wall nucleation appears in the specimen, and the direction of the primary dendrite arm is mussy as proved by the optical figures of the cross section surface shown in Fig. 3g, h. Besides, for the specimens grown at the rates of 50, 200 and 1000 μm/s, Tb-rich precipitates keep the shape of particles and dispersively distribute in the matrix. Therefore, all of the as-cast and directionally solidified specimens possess dual-phase structure containing non-modulated martensite matrix and Tb-rich precipitates. It is also observed that the size of Tb-rich precipitates varies when changing the growth rate (see Fig. 3c, f, i), and the reason may be as follows. The melting temperature of the precipitates is lower than that of the matrix NiMnGa intermetallic. Therefore, the precipitates are formed in the space among the columnar grains or the dendritic grains during the directional solidification process. Therefore, the increasing growth rate leads to smaller space for the growth of Tb-rich precipitates, resulting in the smaller size of them.

Detailed morphologies of the dual-phase alloys are analyzed by TEM images, as shown in Fig. 4. The martensite phase exhibits clear lath-shape morphology. Some hair-like structures can be observed in each lath, as marked by the yellow arrows, and they have been proved as nano-twins [17]. For the as-cast alloy, partial Tb-rich precipitates continuously distribute along the grain boundaries, as shown in Fig. 4b. The thickness of the continuous precipitates is ~ 350 nm. After directional solidification process, granular precipitates are formed instead of the continuous precipitates, as shown in Fig. 4c. The average size of the particles is 2–3 μm. Besides, the lath-shape structure is still quite clear around the continuous and granular precipitates, indicating that the formation of precipitates does not affect the structure of martensite phase, and the completeness of martensite phase remains good. Therefore, the martensitic transformation may be maintained despite the shape change of the precipitates. The crystal structure of Tb-rich precipitates has been analyzed by the selected area electron diffraction (SAED) patterns

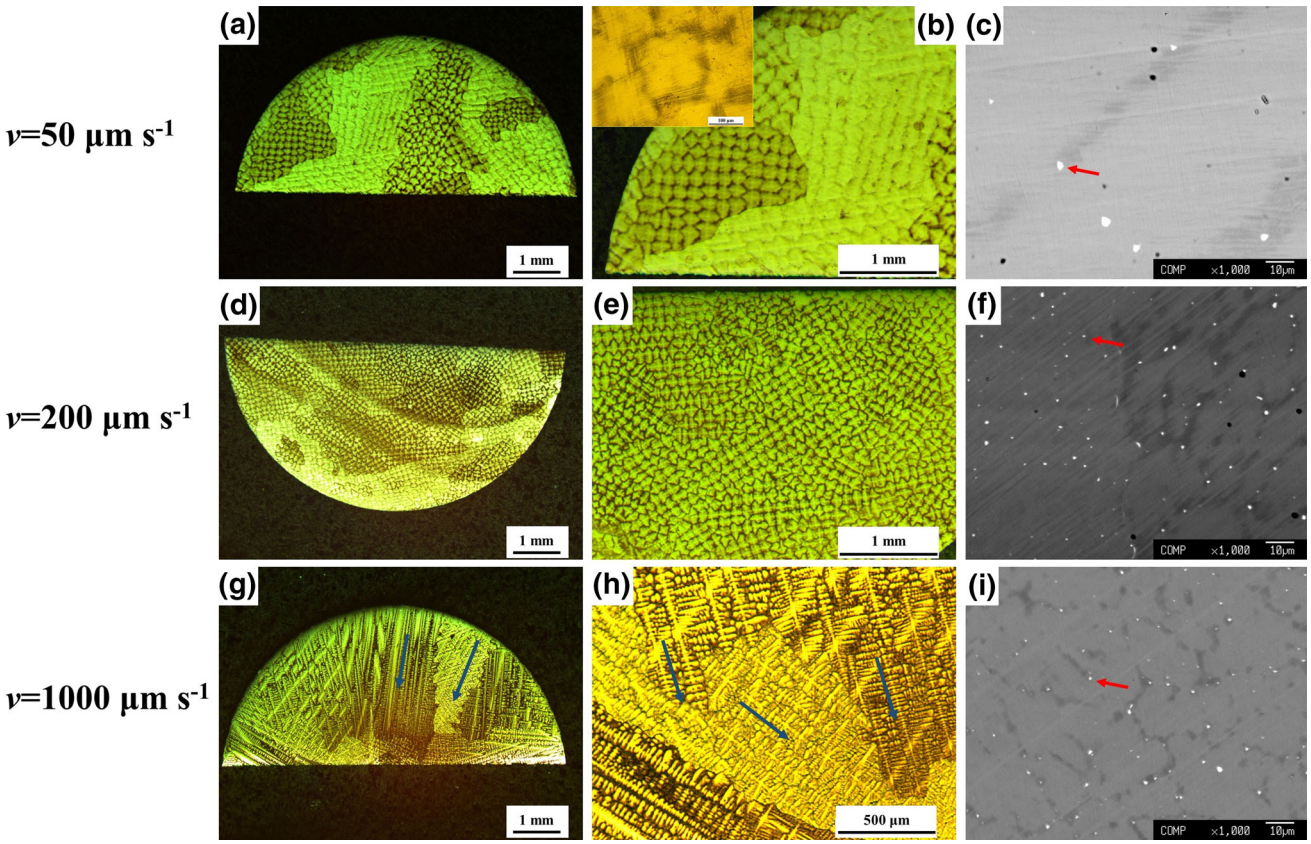

Fig. 3 Optical morphologies and BSEs of $Ni_{50}Mn_{29}Ga_{20.8}Tb_{0.2}$ alloy grown at 50 μm/s (**a–c**), 200 μm/s (**d–f**) and 1000 μm/s (**g–i**)

with the incident electron beam tilted to $[01\bar{1}0]$, $[1\bar{2}1\bar{3}]$ and $[2\bar{1}\bar{1}0]$, respectively, as shown in Fig. 4d–f. SAED images confirm a hexagonal structure similar to that of RNi_4Ga (R = Sm, Gd, Tb) alloys [28]. A rough calculation of the lattice parameters is $a \approx 0.509(4)$ nm and $c \approx 0.417(2)$ nm. The lack of slip systems of the hexagonal structure for the precipitates leads to the significant brittleness of them, so a large amount of the precipitates will significantly deteriorate the ductility. The particulate precipitates can enhance the grain boundaries with lower adhesion, resulting in the improved shape memory effect.

Figure 5 shows the reverse martensitic transformation behavior from the low-temperature martensite phase to the high-temperature austenite phase. For all the as-cast and as-directionally solidified alloys, reverse martensitic transformation is detected as shown by the endothermic peaks during heating process. The anomalous variation tendency of reverse martensitic transformation temperature (T_M, which is chosen to be DSC peak temperature here) and transformation temperature span (T_S) is observed here. T_M gradually decreases from 51.6 °C for the as-cast alloy to 48.7 °C for the alloy grown at 10 μm/s, subsequently to 45.0 °C for the alloy grown at 50 μm/s, and finally to 37.5 °C for the alloy grown at 1000 μm/s. Simultaneously, the endothermic peak slightly shrinks from the as-cast alloy to the alloy grown at 10 μm/s. Subsequently, the peak monotonously broadens with the increasing withdrawal rate, from 5 °C for the alloy grown at 10 μm/s to 37.1 °C for the alloy grown at 1000 μm/s.

Since the initial atomic ratios remain the same for all the rods and energy dispersive spectroscopy analysis has confirmed that the composition remains unchanged after directional solidification process, the evolution of solidification microstructure should give rise to the variation in characteristic temperatures of reverse martensitic transformation. Many investigations have revealed that the martensitic transformation temperature can be significantly shifted by the grain size, and the grain refinement generally leads to the decrease in T_M [29, 30]. Therefore, the refinement in the solidification microstructures from the micro-sized grains to the dendrites contributes to the reduction of T_M in the series of NiMnGaTb alloys. Furthermore, the enlargement in T_S is related to the grain refinement to some extent, because the grain boundaries provide some resistance in the motion of twin boundaries. More importantly, the size of precipitates plays a key role in the broadening of reverse martensitic transformation. It has been proved that the decreasing size of the precipitates can significantly broaden T_S by regulating the matrix–

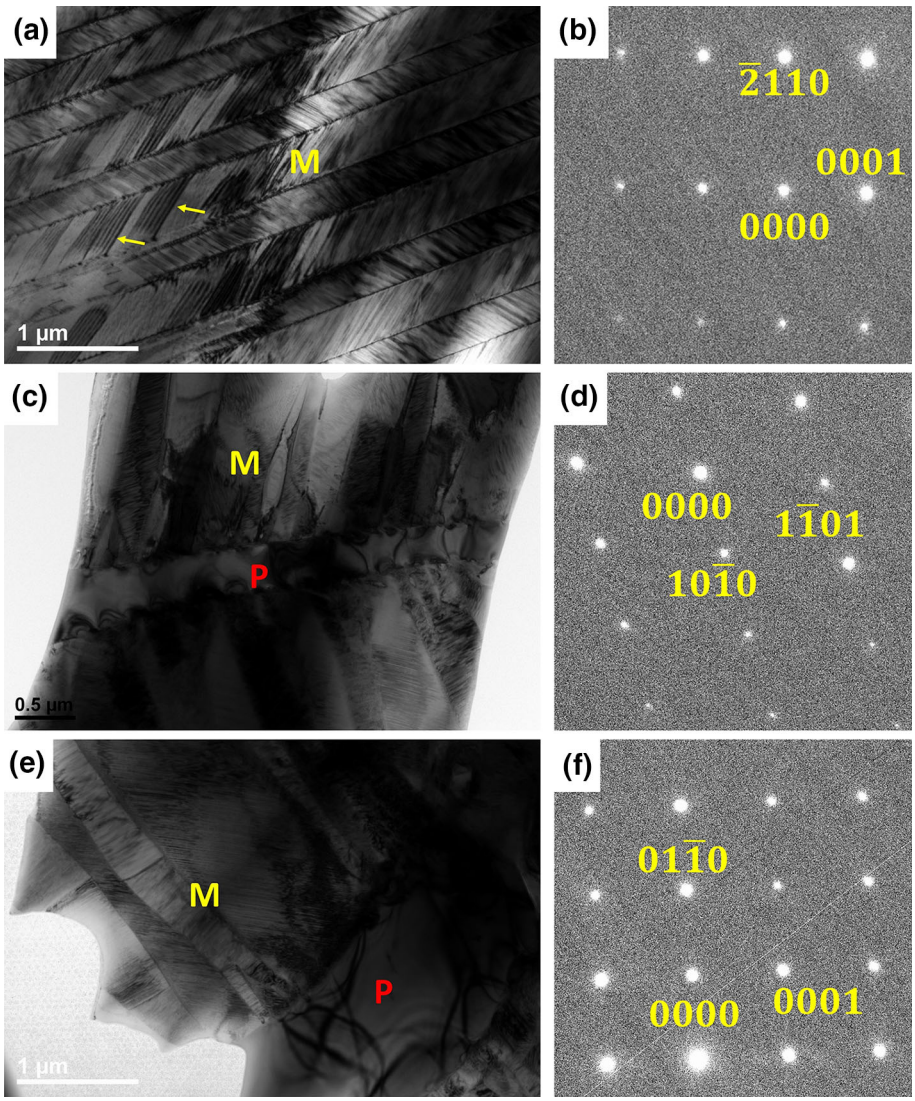

Fig. 4 Bright-field TEM images of as-cast $Ni_{50}Mn_{29}Ga_{20.8}Tb_{0.2}$ alloy (**a**, **c**) and $Ni_{50}Mn_{29}Ga_{20.8}Tb_{0.2}$ alloy (**e**) grown at 50 μm/s. **b**, **d**, **f** are SAED patterns with the incident electron beam tilted to $[01\bar{1}0]$, $[1\bar{2}1\bar{3}]$ and $[2\bar{1}\,\bar{1}0]$, respectively

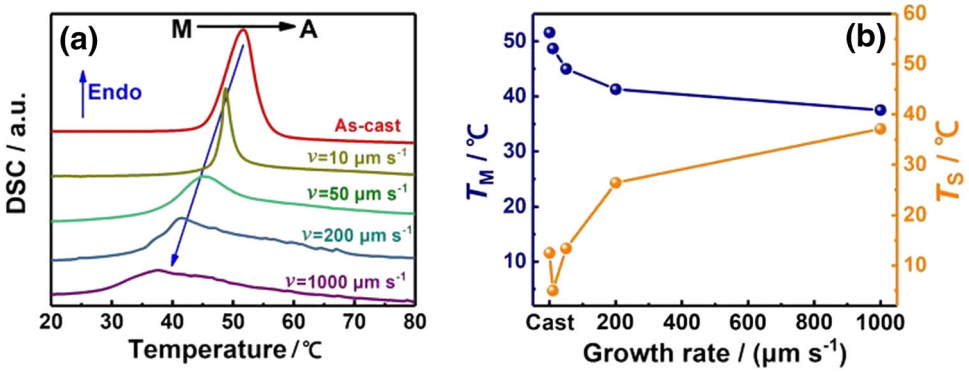

Fig. 5 Heating DSC curves of as-cast and directionally solidified $Ni_{50}Mn_{29}Ga_{20.8}Tb_{0.2}$ alloys (**a**) and summary of T_M and T_S (**b**)

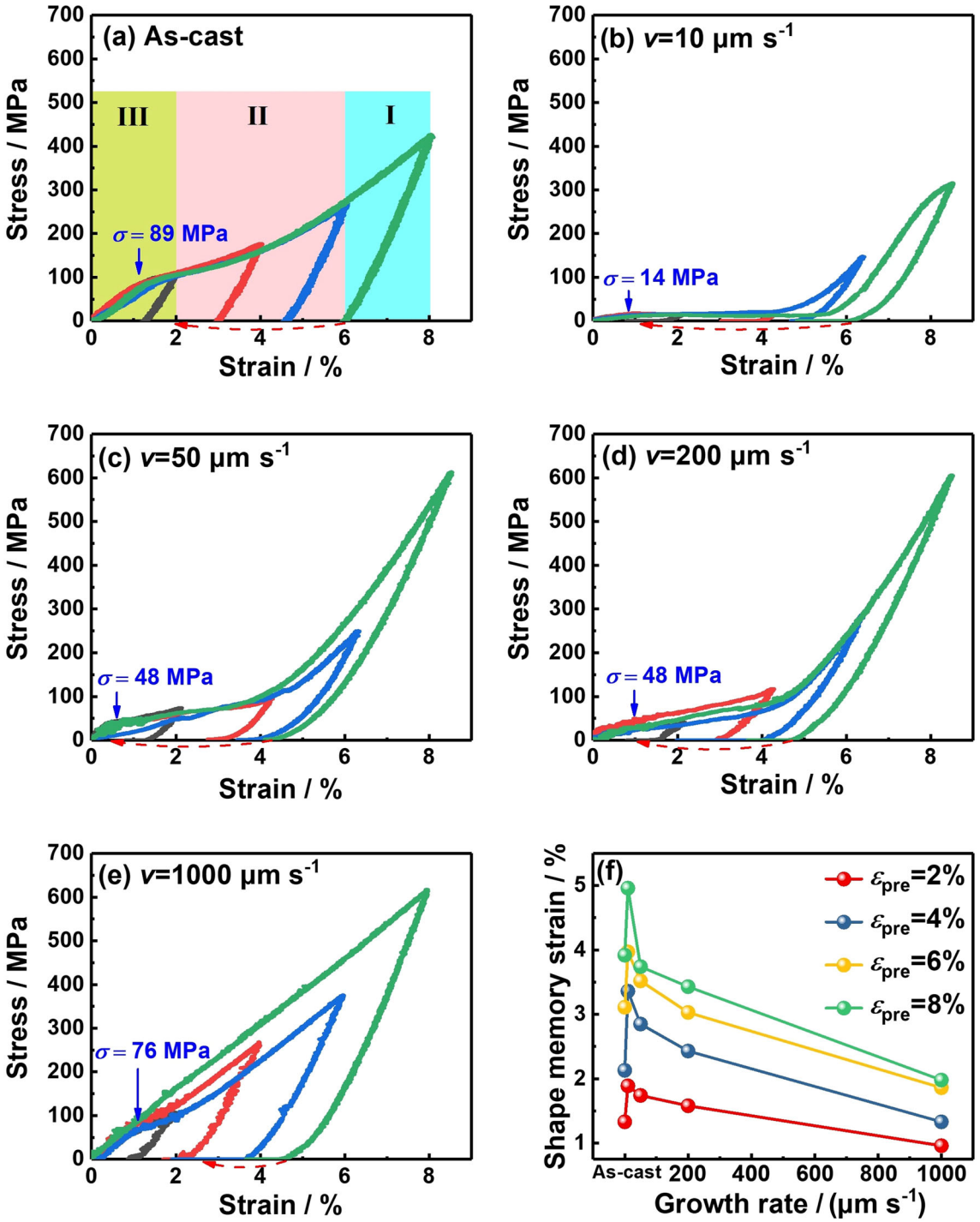

Fig. 6 Compressive stress–strain curves under pre-strain of 2%, 4%, 6% and 8% for as-cast (**a**) and directionally solidified (**b**–**e**) $Ni_{50}Mn_{29}Ga_{20.8}Tb_{0.2}$ alloys and summary of shape memory strain (**f**)

precipitate interface. The coherent or semi-coherent interface could induce lattice distortion around the precipitates, forming local internal stress field. This results in the shift of martensitic transformation temperature in local regions with different intensities of local stress field, and thus, the transformation span is broadened [30]. For the Bridgman directional solidification technology, the temperature gradient does not change much when the heat preservation temperature remains the same. Therefore, the cooling rate is proportional to the withdrawal rate, and increasing withdrawal rate leads to larger cooling rate, resulting in the decreasing size and higher density of granular precipitates,

as proved by BSE figures shown in Fig. 3. Even though the martensitic transformation temperature is decreased and the span is broadened, the martensitic transformation is still reserved despite the evolution of the solidification microstructure. Therefore, the temperature of 10 °C is selected to measure the shape memory effect since the matrix of all the specimens should be martensite phase at this temperature.

The shape memory effects of all the alloys are determined by compression tests. The pre-strains of 2, 4, 6 and 8% are, respectively, applied to each specimen, and the corresponding stress–strain curves are exhibited in Fig. 6. The dotted lines represent the recovery strain after heating at 200 °C for 10 min. The curve consists of three parts, the residual strain which recovers after unloading (ε_r, part I), shape memory strain which recovers after heating (ε_{sme}, part II) and permanent strain which keeps unrecovered after heating (ε_p, part III). Among the three parameters (ε_r, ε_{sme} and ε_p), ε_{sme} is a key parameter to evaluate the shape memory effect of the alloys, so ε_{sme} of as-cast and as-directionally solidified $Ni_{50}Mn_{29}Ga_{20.8}Tb_{0.2}$ alloys has been investigated; the results are summarized in Table 1, and the evolution of ε_{sme} under different ε_{pre} for the specimens is exhibited in Fig. 6f. For the isotropic as-cast alloy, ε_{sme} gradually increases from 1.33% under the pre-strain of 2–3.92% under the pre-strain of 8%. Compared with the ternary NiMnGa as-cast alloy with similar atomic percentages, the value of ε_{sme} of the dual-phase alloy is a bit lower than that of the single-phase alloy under the same ε_{pre}. However, when the pre-strain exceeds 6%, the single-phase samples were thoroughly broken after heat treatment due to the strong intrinsic brittleness of the single-phase NiMnGa alloys. The dual-phase microstructure derived from Tb doping significantly increases the ductility of the alloys and allows their operation under larger pre-strain conditions. Moreover, the compressive stress required to trigger the reorientation of twins (marked as σ) in the as-cast specimen is about 89 MPa, as marked in Fig. 6a. For the directionally solidified alloys, even though the distribution of precipitates transforms to be dispersive, the ductilities of the specimens are still sufficient to undertake the pre-strain as large as 8%. And ε_{sme} generally exhibits a decreasing tendency with the increasing withdrawal rate. When the withdrawal rate is 10 μm/s, ε_{sme} is significantly improved compared with that of the as-cast alloy, and the largest shape memory strain can achieve 4.96% under ε_{pre} of 8%. Besides, σ is only 14 MPa according to the stress–strain curves. This should be attributed to the single-crystal structure, i.e., the absence of grain boundaries allows the twins re-orient to the same direction under external stress, and the stress required to trigger the twin re-orientation is lower because of the weakening of stress dispersion by the grain boundaries. When the withdrawal rate increases to 50 and 200 μm/s, ε_{pre} is lower than that in v = 10 μm/s specimens but is still considerable. σ is $\sim$ 48 MPa for both alloys due to the same preferred orientation, but ε_{sme} is degraded in v = 200 μm/s specimens because of the longer secondary dendritic arms. When the withdrawal rate further increases to 1000 μm/s, ε_{sme} is seriously degraded due to the mussy dendrite morphology, and σ is simultaneously increased to $\sim$ 76 MPa which is close to that in the as-cast alloy, indicating the loss of preferred orientation in this specimen. Results above indicate that the directional solidification technology can effectively enhance ε_{sme} and decrease σ via the realization of preferred orientation, and the maximal ε_{sme} and minimum σ can reach 4.96% and 14 MPa, respectively. The formation of dendrite morphology degrades the shape memory strain, and ε_{sme} decreases with the growth of secondary dendritic arms.

Table 1 Recoverable reorientation strains of martensitic variants of $Ni_{50}Mn_{29}Ga_{20.8}Tb_{0.2}$ alloys with different pre-strains

Specimen condition	ε_{sme}/%			
	ε_{pre} = 2%	ε_{pre} = 4%	ε_{pre} = 6%	ε_{pre} = 8%
As-cast	1.33	2.13	3.11	3.92
v = 10 μm/s	1.89	3.36	3.97	4.96
v = 50 μm/s	1.74	2.85	3.52	3.74
v = 200 μm/s	1.58	2.43	3.03	3.43
v = 1000 μm/s	0.96	1.33	1.86	1.98

4 Conclusion

Different microstructures containing single-crystal microstructure, preferred dendrite microstructure and mussy dendrite microstructure were obtained in directionally-solidified NiMnGaTb alloys via regulating the withdrawal rate. The precipitates dispersively distribute in the martensite matrix for the directionally-solidified alloys, and the grains and precipitates are gradually refined with the increasing withdrawal rate. Accordingly, the reverse martensitic transformation gradually shifts to lower temperatures and the temperature span is significantly broadened. The shape memory effect is remarkably enhanced in the directionally-solidified specimens with preferred orientation, and the maximal ε_{sme} and minimum σ can reach 4.96% and 14 MPa in v = 10 μm/s specimens, respectively. When the withdrawal is over a critical value, the formation of dendrite morphology degrades the shape memory strain due to the growth of secondary dendritic arms.

Acknowledgements This work was supported by the National Natural Science Foundation of China (NSFC) under Grant Nos. 513311001, 51520105002, 51601007, and 51601008 and the China Postdoctoral Science Foundation Funded Project under Grant Nos. 2017M610738 and 2018T110026.

References

[1] K. Ullakko, J.K. Huang, C. Kanter, V.V. Kokorin, R.C. O'Handley, Appl. Phys. Lett. 69 (1996) 1966–1968.
[2] H. Hua, J.M. Wang, C.B. Jiang, H.B. Xu, Scripta Mater. 124 (2016) 142–145.
[3] A. Sozinov, N. Lanska, A. Soroka, W. Zou, Appl. Phys. Lett. 102 (2013) 021902.
[4] M. Chmielus, X.X. Zhang, C. Witherspoon, D.C. Dunand, P. Müllner, Nat. Mater. 8 (2009) 863–866.
[5] H. Zhang, T.L. Zhang, C.B. Jiang, Smart Mater. Struct. 21 (2012) 055014.
[6] T.L. Zhang, C.B. Jiang, H.B. Xu, J.Q. Mao, J. Appl. Phys. 101 (2007) 034511.
[7] T.L. Zhang, C.B. Jiang, X.L. Liu, H.B. Xu, Smart Mater. Struct. 14 (2005) N38–N41.
[8] A. Smith, C.R.H. Bahl, R. Bjørk, K. Engelbrecht, K.K. Nielsen, N. Pryds, Adv. Energy Mater. 2 (2012) 1288–1318.
[9] O. Gutfleisch, M.A. Willard, E. Brück, C.H. Chen, S.G. Sankar, J.P. Liu, Adv. Mater. 23 (2011) 821–842.
[10] Y.Y. Wu, J.M. Wang, J. Zhang, Intermetallics 89 (2017) 100–104.
[11] C. Biswas, R. Rawat, S.R. Barman, Appl. Phys. Lett. 86 (2005) 202508.
[12] J.M. Wang, Q. Yu, K.Y. Xu, C. Zhang, Y.Y. Wu, C.B. Jiang, Scripta Mater. 130 (2017) 148–151.
[13] Z. Yang, D.Y. Cong, L. Huang, Z.H. Nie, X.M. Sun, Q.H. Zhang, Y.D. Wang, Mater. Des. 92 (2016) 932–936.
[14] Z.J. Jiang, Y.Y. Wu, J.W. Wang, C.B. Jiang, J. Iron Steel Res. Int. 24 (2017) 711–717.
[15] X. Moya, E. Defay, V. Heine, N.D. Mathur, Nature Phys. 11 (2015) 202–205.
[16] W. Sun, J. Liu, B.F. Lu, Y. Li, A.R. Yan, Scripta Mater. 114 (2016) 1–4.
[17] Y.Y. Wu, J.M. Wang, C.B. Jiang, H.B. Xu, Mater. Sci. Eng. A 646 (2015) 288–293.
[18] K. Tsuchiya, A. Tsutsumi, H. Ohtsuka, M. Umemoto, Mater. Sci. Eng. A 378 (2004) 370–376.
[19] Y.Y. Wu, J.M. Wang, H. Hua, C.B. Jiang, H.B. Xu, J. Alloy. Compd. 632 (2015) 681–685.
[20] L. Gao, G.F. Dong, Z.Y. Gao, W. Cai, J. Alloy. Compd. 520 (2012) 281–286.
[21] X. Zhang, J.H. Sui, Z.L. Yu, W. Cai, J. Alloy. Compd. 509 (2011) 8032–8037.
[22] Y.Y. Wu, L. Fang, C.Z. Meng, Y.J. Chen, J.M. Wang, J.H. Liu, T.L. Zhang, C.B. Jiang, Mater. Res. Lett. 6 (2018) 327–332.
[23] L. Gao, J.H. Sui, W. Cai, Z.Y. Gao, Solid State Commun. 149 (2009) 257–260.
[24] L. Gao, Z.Y. Gao, W. Cai, L.C. Zhao, Mater. Sci. Eng. A 438–440 (2006) 1077–1080.
[25] J.H. Sui, X. Zhang, X.H. Zheng, Z.Y. Yang, W. Cai, X.H. Tian, Scripta Mater. 68 (2013) 679–682.
[26] C.Z. Meng, Y.Y. Wu, C.B. Jiang, Mater. Des. 130 (2017) 183–189.
[27] X. Zhang, J.H. Sui, X.H. Zheng, Z.Y. Yang, W. Cai, Mater. Sci. Eng. A 597 (2014) 178–182.
[28] D.A. Joshia, C.V. Tomy, R. Nagarajan, S.K. Malik, J. Magn. Magn. Mater. 313 (2007) 151–156.
[29] Y.Y. Wu, J.M. Wang, Y.K. He, H.C. Wu, C.B. Jiang, H.B. Xu, Acta Mater. 104 (2016) 91–100.
[30] Y.Y. Wu, J.M. Wang, C.B. Jiang, H.B. Xu, Intermetallics 97 (2018) 42–51.